

Distributed range adaptation in human parietal encoding of numbers

Arthur Prat-Carrabin^{1,*}, Gilles de Hollander^{2,3*}, Saurabh Bedi^{2,3}, Samuel J. Gershman¹, and Christian C. Ruff^{2,3}

¹Department of Psychology and Center for Brain Science, Harvard University, Cambridge, MA, USA

²Zurich Center for Neuroeconomics, Department of Economics, University of Zurich, Switzerland

³University Research Priority Program (URPP), Adaptive Brain Circuits in Development and Learning, University of Zurich, Zurich, Switzerland

*equal contribution

**arthurpc@fas.harvard.edu, gilles.de.hollander@gmail.com*

Abstract

The brain represents magnitudes through the collective activity of neural populations, whose non-monotonic tuning properties determine the nature and precision of the population neural code^{1–9}. Whether and how this code adapts to changes in the statistics of the encoded magnitudes remains unknown. Here we probe the adaptation of the encoding of numbers in human parietal cortex, using functional MRI during a numerosity-estimation task in which we vary the range of possible numbers. Tracking the tuning properties of number-sensitive populations as the range changes, we show that their receptive fields shift and scale in adaptation to the range, following a structured and predictable pattern. This distributed range adaptation implements efficient coding^{10–13} dynamically: the resulting precision of the neural code varies with the range and is accompanied by corresponding changes in behavioral precision. At the participant level, the degree of neural tuning adaptation significantly predicts the change in behavioral variability. Our results extend static sensory efficient coding to the adaptive representation of abstract magnitudes, via an explicit neural mechanism of distributed range adaptation that may be a canonical property of neural encoding circuits.

Efficient coding prescribes that the brain's representational resources should be optimally allocated across the stimuli that one may encounter^{10–13}. Accordingly, neural tuning curves in various sensory systems are efficiently adapted to the statistics of the sensory stimuli that they encode^{14,15}. Yet in natural environments, stimulus statistics typically fluctuate over time and across contexts. For coding to remain efficient, neural representations must therefore be flexible and adapt to these changes. One form of such flexibility is 'range adaptation', whereby neurons with monotonic tuning modulate their gains to effectively map the current stimulus range onto their limited response range^{16–19}. However, across many species and sensory modalities, the most widespread form of representation relies on populations of neurons with non-monotonic, bell-shaped tuning curves (e.g., orientations¹, motion direction³, spatial frequency⁴, sound frequency², whisker angle⁵, and numerosity⁶, among others⁷). The notion of monotonic range adaptation has no clear analogue in these distributed codes. Hence, although such networks are the predominant form of neural representation, it is largely unknown whether and how they adapt to changes in stimulus statistics.

There is, however, some evidence that distributed neural representations are not static: experimental studies have exhibited shifts of neuronal tuning curves, when a stimulus is the locus of attention or when it is repeatedly presented, and in the encoding of reward intervals^{20–26}. Here we propose that this flexibility more generally enables neural populations to adapt to changing stimulus statistics. Specifically, we hypothesize that when the range of possible stimuli changes, the receptive fields of the encoding neural populations shift and scale, in order to efficiently remap neural representations to cover the new range. We call this mechanism 'distributed range adaptation'. It involves the concerted adaptation of the entire sensory network to a change in the range of stimuli. Such neural mechanism could be a property shared by many sensory circuits, enabling the flexible allocation of processing resources to achieve optimal behavioral sensitivity, in line with the principle of efficient coding.

Here we examine our proposal in the context of number representation in humans. Previous research on neural tuning and perception has often focused on the sensory encoding of physical attributes of stimuli (e.g., orientations). Yet many natural decisions are based on abstract quantities that are not directly rooted in physical magnitudes^{7,27–30}. In particular, the ability to represent and act upon numerical information is a fundamental skill shared across a wide evolutionary range of species, from primates to squids^{31–33}. In humans, this 'number sense' is supported by number-sensitive neurons that exhibit bell-shaped receptive fields centered on their preferred numerosities^{33–37}. Recent behavioral evidence shows that the perception of numbers by humans exhibits larger errors when the range of possible numbers in a task increases, suggesting a dynamic and efficient adaptation of number representations^{38–41}. Whether and how this reflects a reallocation of encoding resources at the neural level is unknown, but shifts in the tuning of number-sensitive populations have been reported^{24,42}, making number representation a good candidate to probe distributed range adaptation in humans.

We investigate our proposal in 39 participants tasked with estimating the number of dots in visual displays while undergoing 3T functional MRI, as we manipulate the range of the distribution of numbers (the prior). Neurocomputational modeling of the fMRI data with numerical population receptive field (nPRF) models³⁵ enables us to identify

tuning properties of numerosity-selective populations in the intraparietal sulcus (IPS), quantify their changes across priors, and test our hypotheses. We find that the preferred numerosities of the neural populations shift across priors in a way that closely aligns with the quantitative predictions of our proposal. In addition, the widths of the population receptive fields broaden with the width of the prior. Across priors, the encoding populations thus reorganize in a structured fashion to efficiently cover the relevant range, consistent with distributed range adaptation.

Identifying the tuning properties of neural populations also enables us to quantify the representational acuity of the neural population code. With a wider prior, we find that the neural encoding is less precise, consistent with the hypothesis that distributed range adaptation implements efficient coding. The fMRI data, moreover, predicts individual variations in behavior. Specifically, the individual changes in neural encoding across priors predict the individual changes in response precision, supporting the behavioral relevance of the dynamic efficient neural coding evident in the parietal populations. Finally, we also show that within the context of a given prior, the neural data is predictive of individual variations in how participants compress larger numbers (Weber's law): participants whose neural precision decreases faster with large numbers provide less precise estimates for these numbers.

Overall, our results extend the principles of sensory efficient coding to the dynamic adaptation of abstract numerical representations in humans, mediated by distributed range adaptation as a possible canonical mechanism of sensory circuits. Our work also highlights how encoding models for fMRI can be leveraged to probe the neural substrates of cognitive representations, and to establish links, at the individual level, between neural activity and decision-making.

Behavioral variability and neural efficient coding

On each trial of a numerosity-estimation task conducted in an MRI scanner, we present participants with a cloud of dots for 600ms and ask them to provide their best estimate of the number of dots (Fig. 1a). This number is randomly sampled from a uniform prior, whose width differs in two experimental conditions. In the 'Narrow' condition, the number of dots ranges from 10 to 25, while in the 'Wide' condition it ranges from 10 to 40. The prior width in the Wide condition is thus twice as large as in the Narrow condition (Fig. 1c; see Methods).

The variability in participants' estimates is greater in the Wide condition than in the Narrow condition (Fig. 1b), replicating previous results³⁸. This increased variability suggests a more imprecise representation of the numbers with the Wide prior. In turn, this points to an adaptive and dynamic implementation of efficient coding, in which the allocation of representational resources optimally adjusts to the current range of numbers, resulting in lower precision for each number under the Wide prior.

We thus hypothesize that the observed changes in behavioral variability reflect changes in neural encoding of numerosity. Numerosity-sensitive neural populations have bell-shaped receptive fields characterized mainly by their preferred numerosities and their widths. We hypothesize that when the prior changes, the preferred numerosities shift and the widths of the receptive fields scale, efficiently adapting to the new distribution.

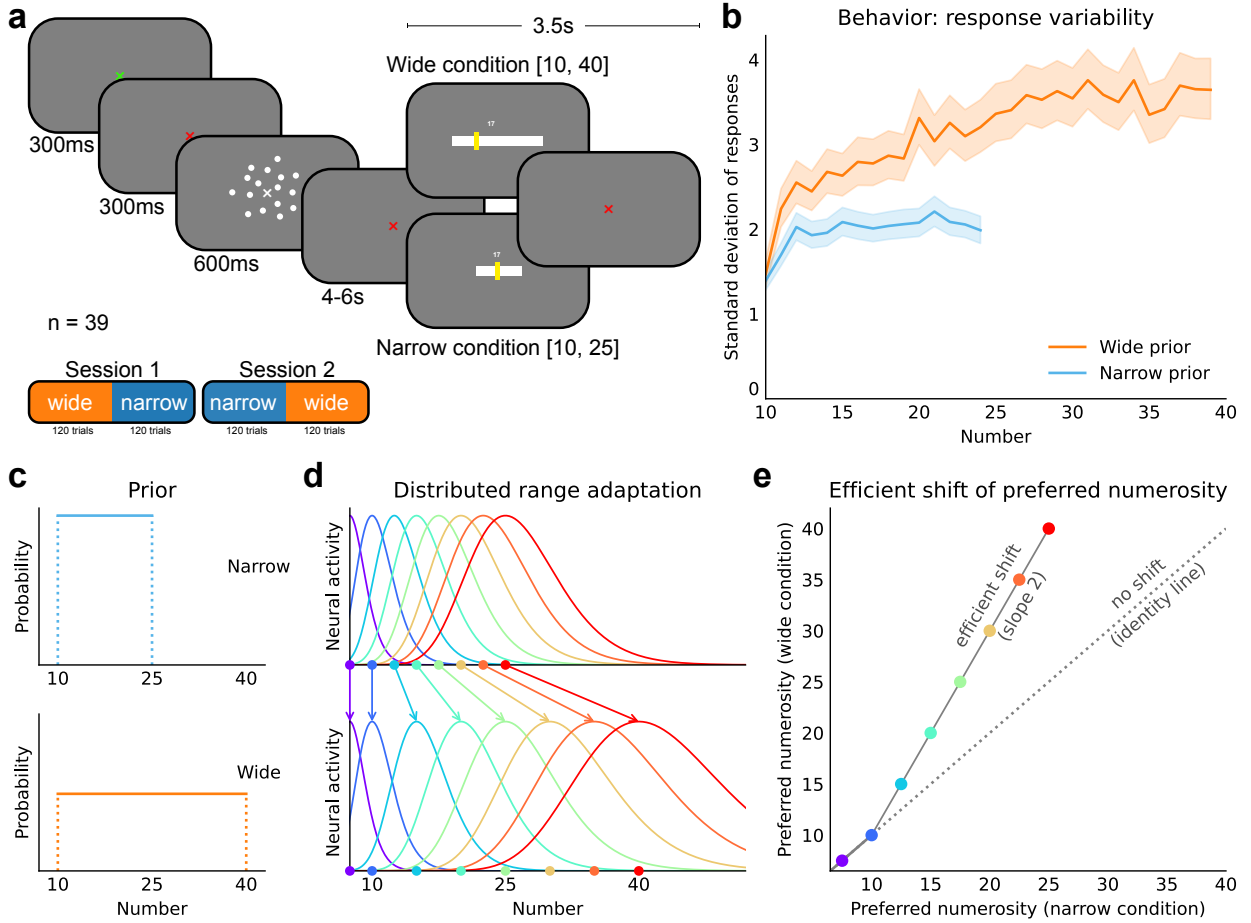


Fig. 1: Behavioral task and illustration of distributed range adaptation. **a**, Numerosity-estimation task conducted in the MRI scanner. The participant is asked to estimate the number of dots in a cloud presented for 600ms. This number is randomly sampled from a Narrow or a Wide range (see **c**), and each participant experiences twice each prior across two experimental sessions. **b**, Standard deviation of the participants' responses as a function of the correct number, in the two conditions. Participants are more variable with the Wide prior. Shaded areas show the 5%-95% credible intervals (see [Methods](#)). **c**, Narrow and Wide uniform priors used in the two conditions of the experiment. The Wide prior (10-40) is twice as large as the Narrow prior (10-25). **d**, Schematic illustration of distributed range adaptation: the populations' receptive fields in the Narrow condition (top panel) are re-allocated in the Wide condition (bottom panel), to efficiently cover the wider range. Hence the receptive fields shift and widen, and over the Narrow range the preferred numerosities in the Wide vs the Narrow condition describe a line of slope 2, the ratio of the prior widths (**e**).

Specifically, our hypothesis is that the distribution of preferred numerosities in the Narrow condition expands in the Wide condition, such that they correspond to the same quantiles across priors, a collective adjustment that we call distributed range adaptation (Fig. 1d). Because both priors are uniform and the Wide prior is twice as large as the Narrow one,

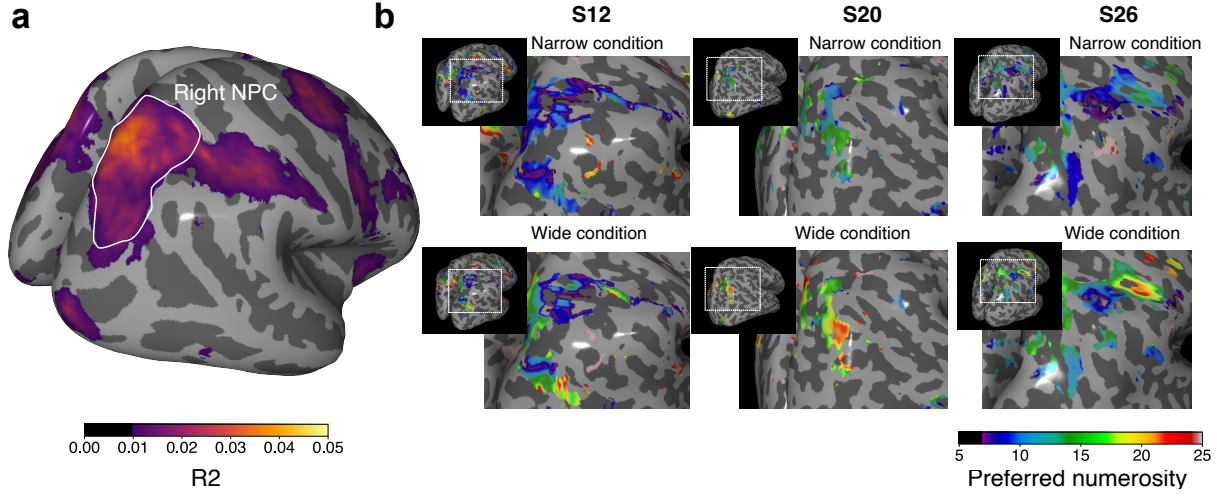


Fig. 2: Maps of numerical population receptive fields show shifts of voxels' preferred numerosities. **a**, Explained variance (R^2) of the nPRF 'free-shift' model across 39 participants in *fsaverage*-space. The outlined area indicates the right NPC mask used in all analyses. **b**, Individual maps of preferred numerosities in the two conditions. From the Narrow to the Wide condition, preferred numerosities generally shift upwards. In the 'free-shift' model, there are no constraints on the relationship between the two conditions, and each preferred-numerosity parameter of each voxel in each condition is fitted separately.

distributed range adaptation implies a linear relationship with a slope of 2 between a population's preferred numerosities in the Wide and Narrow conditions (Fig. 1e). For instance, if a population's preferred numerosity is 15 in the Narrow condition, then we predict it will shift to 20 in the Wide condition (since 20 is twice as far from the lower bound 10 as is 15). This 'efficient-shift' linear relationship is a quantitative prediction that puts a strong constraint on the receptive fields we should observe across priors. Note that distributed range adaptation is not in itself a prediction of traditional efficient coding; rather, it is a proposed mechanism to flexibly implement efficient coding in sensory networks.

While the preferred numerosity of a neural population indicates the number that elicits its strongest response, its width determines its specificity. When the prior doubles in size, as in our experiment, one might assume that the receptive-field widths should also double in size. But if both the preferred numerosities and the widths scale with a factor 2 between the Narrow and Wide conditions (all else being equal), then the imprecision of the encoding, as measured for instance by the standard deviation of estimates, should scale by the same factor. Previous studies have shown, however, that this is not the case; instead, the imprecision decreases sublinearly with the width of the prior, and thus participants are *relatively* more precise with wider priors^{38,39}. For this reason, we do not expect the widths to double in size; if they do expand, we expect that it should be by a factor lower than 2.

Numerical population receptive fields

We fit models of numerical population receptive fields (nPRFs) to the single-trial BOLD responses per voxel at the time of the presentation of the stimulus, specifically in the

intraparietal sulcus (IPS; Fig. 2). The region of interest (ROI) we focus on is the right numerical parietal cortex (rNPC) identified as having the most pronounced number fields in several previous studies^{35,43–46} (Fig. 2a; see Methods). Each nPRF model specifies a voxel’s average activity as a unimodal function of the encoded number, parameterized by its preferred numerosity, its width, its baseline activity, and its amplitude (specifically, in line with previous results, we choose Gaussian functions in logarithmic space; see Methods). We fit different nPRF models corresponding to different hypotheses and we report the proportions of voxels in the ROI with positive cross-validated variance explained ($\text{cv}R^2 > 0$; nPRF parameters are only reported for such ‘signal’ voxels). We use $\text{cv}R^2$ as a voxelwise model comparison technique because it balances model flexibility and generalizability with minimal assumptions⁴⁷. By evaluating performance on held-out data, $\text{cv}R^2$ automatically penalizes overfitting, ensuring that improvements in fit from additional parameters generalize to unseen data. Conversely, improvements in fit with fewer parameters suggests that the implied constraints are verified in data.

Efficient shifts of the receptive fields

First, we look at the voxels’ preferred numerosities. Fixing all the other parameters, we let the preferred numerosities of each voxel in the Narrow and Wide conditions be free parameters, μ_n and μ_w (‘free-shift’ model). The two are strongly correlated (participants pooled: $r = 0.67$, $P < 10^{-320}$, $N = 8008$; across participants: average $r = 0.74$, interquartile range (IQR): 0.63–0.88). Thus, the neural populations tuned to larger numbers in the Narrow condition are also tuned to larger numbers in the Wide condition. However, the maps of preferred numerosities in each condition suggest that for a given voxel, the preferred numerosity in the Wide condition is larger than that in the Narrow condition (as shown in Figure 2b for three representative participants). Indeed, the relation between a voxel’s preferred numerosities across the two conditions is not well described by the identity function, except for small numerosities; most voxels with preferred numerosities above 10 in the Narrow condition shift to higher preferred numerosities in the Wide condition (i.e., $\mu_w > \mu_n$; Fig. 3a,b). This increase is observed in most participants: for 37 out of 39 participants, the across-voxels median preferred numerosity is larger in the Wide condition than in the Narrow condition (Fig. 3c; across-participants paired t-test of equality of the medians in the two conditions: $t(38) = 8.98$, $P = 6 \times 10^{-11}$). Overall, the preferred numerosities of 84% of voxels increase in the Wide condition as compared to the Narrow condition (Fig. 3d).

The voxels’ locations across conditions are remarkably well described by the hypothesis of distributed range adaptation (compare Fig. 3a,b to Fig. 1e). The preferred numerosities in the Wide vs. Narrow conditions are close to a line of slope 2, as hypothesized, when the preferred numerosity in the Narrow condition is above 10 (the lower bound of both priors). For example, voxels whose preferred numerosities are close to 15 in the Narrow condition indeed exhibit preferred numerosities on average close to 20 in the Wide condition (e.g., μ_w for voxels with $\mu_n \in [14.5, 15.5]$ is on average 20.05; standard error of the mean (sem): 0.19). An informal description of distributed range adaptation is that the voxels’ preferred numerosities “spread out” to cover the wider prior, which is what we observe.

As for preferred numerosities below 10, we note that if participants hold subjective

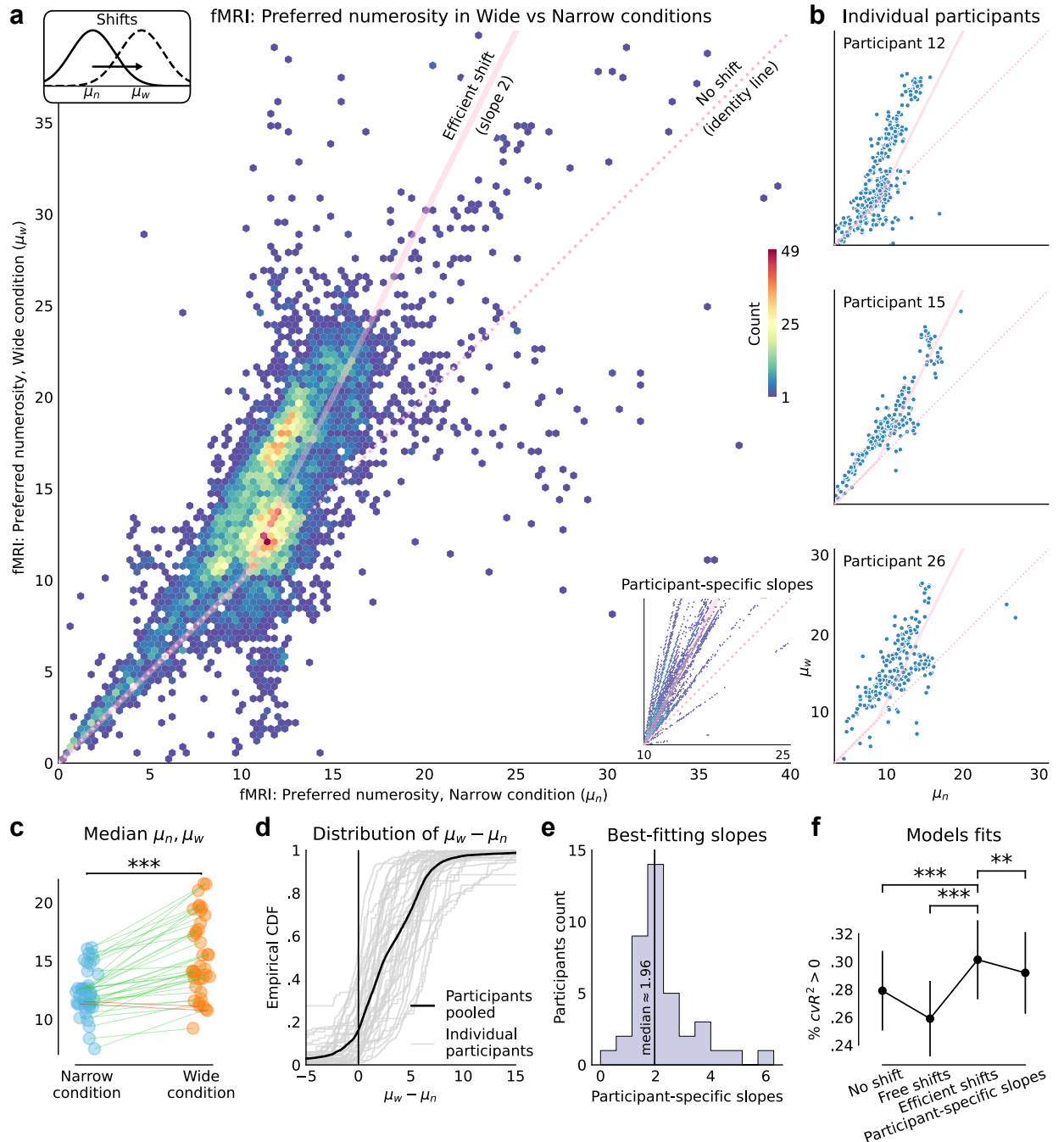


Fig. 3: Efficient shifts of neural receptive fields across priors. **a**, Distribution of the voxels pairs of best-fitting preferred-numerosity parameters (μ_n, μ_w) in the Wide vs. Narrow conditions (participants pooled, ‘free-shift’ fMRI model). The distribution better aligns with the efficient-shift prediction of distributed range adaptation (transparent pink line) than with the identity function (dotted pink line). 1.94% of outlier voxels not shown (μ_n or $\mu_w > 40$). *Inset:* Same distribution, with the ‘participant-specific slopes’ model. **b**, Preferred numerosities in the Wide vs. Narrow conditions for three representative participants (‘free-shift’ model). Pink lines as in **a**. (caption continued on next page)

Fig. 3: (cont.) **c**, Median preferred numerosities for each participant in the Narrow (left) and Wide (right) conditions. A green (resp., red) line indicates that the participant's median preferred numerosity in the Wide condition is greater (resp., lower) than in the Narrow condition. **d**, Empirical cumulative distribution of the difference between each voxel's preferred numerosities in the Wide and Narrow condition, $\mu_w - \mu_n$, for each participant (gray lines) and for the participants pooled (black line). For a majority of voxels this difference is positive, i.e., most voxels' receptive fields shift towards larger values in the Wide condition. **e**, Distribution of the slope parameter across participants ('participant-specific slopes' model). The slope parameter is distributed around 2, the value predicted by distributed range adaptation. **f**, Across-participants average of the proportion of voxels with positive cross-validated variance explained ($\text{cv}R^2 > 0$) for (from left to right) the model with no shifts in the voxels' preferred numerosities, the model with free unrestricted shifts (shown in **a**), the 'efficient-shift' model with a slope of 2 (predicted by distributed range adaptation), and the model with participant-specific slopes (inset of **a**). The 'efficient-shift' model outperforms the other three. Error bars show ± 1 standard error of the mean. ***: $P < 0.001$, **: $P < 0.01$.

priors that are mixtures of the correct prior in each condition and of a constant distribution (e.g., a long-term prior), then the quantiles below 10 are identical across the two conditions. In this case our hypothesis implies that the preferred numerosities below 10 should not change across conditions. We find that the identity function indeed characterizes reasonably well the data when preferred numerosities are below 10 (we consider other hypotheses, which do not yield better fits; see Supplementary Information). As for larger numbers, only 2.4% of voxels have preferred numerosities greater than 25 in the Narrow condition; due to this scarcity of data, we do not investigate additional assumptions for these voxels.

To further test our hypothesis, we fit an 'efficient-shift' model which enforces the predicted relationship between a voxel's preferred numerosities in the two conditions (i.e., μ_n is a free parameter and $\mu_w = 10 + 2(\mu_n - 10)$ if $\mu_n \geq 10$, otherwise $\mu_w = \mu_n$). We emphasize that this is a strong constraint that considerably reduces the number of nPRFs parameters. It yields, however, a better cross-validated fit than the unconstrained, 'free-shift' model considered thus far (with a significant increase of the proportion of voxels with $\text{cv}R^2 > 0$; across-participants paired t-test of equality of the proportions: $t(38) = 8.26$, $P = 5 \times 10^{-10}$). It also fits significantly better than a 'no-shift' model that enforces the identity constraint ($\mu_n = \mu_w$; Fig. 3f; $t(38) = 3.63$, $P = 8 \times 10^{-4}$). Hence from one prior to the other, the preferred numerosities of the encoding neural populations shift in a way that is *quantitatively* consistent with distributed range adaptation.

We also consider the possibility that different participants may adjust differently to the distributions. Specifically, we fit a 'participant-specific slopes' model, similar to the 'efficient-shift' model except that the slope is not fixed at 2: it is instead a free parameter for each participant, which we denote by r_μ (i.e., $\mu_w = 10 + r_\mu(\mu_n - 10)$ if $\mu_n \geq 10$, else $\mu_w = \mu_n$; see lower-right inset in Fig. 3a). We find that this slope parameter is distributed (across participants) around 2 (median: 1.96, mean: 2.25, sem: 0.19; Fig. 3e), and the mean best-fitting value is significantly different from 1 (t-test $t(38) = 6.73$, $P = 5.7 \times 10^{-8}$),

but not from 2 ($t(38) = 1.36, P = 0.18$). Moreover, despite this model's flexibility, it fits significantly worse than the more constrained 'efficient-shift' model whose slope is fixed at 2 (Fig. 3f; one-sided paired t-test $t(38) = 2.59, P = 7 \times 10^{-3}$). In other words, assuming for all the participants a slope of 2, the value implied by distributed range adaptation, yields a better and more parsimonious account of the data.

Wider receptive fields with the wider prior

We now turn to the widths of the receptive fields. We start from the 'efficient-shift' model and let the widths of each voxel's receptive field in the two conditions be free parameters, σ_n and σ_w . The two widths are significantly correlated (participants pooled: $r = 0.23, P = 2 \times 10^{-108}, N = 8827$; across participant: average $r = 0.55$, IQR: 0.31-0.89). For a majority of participants (32 out of 39), the median width (across voxels) in the Wide condition is larger than in the Narrow condition (paired t-test of equality: $t(38) = 6.27, P = 2 \times 10^{-7}$; Fig. 4c). Overall, the widths of 77% of voxels increase in the Wide condition as compared to the Narrow condition (Fig. 4d).

Closer examination of the distribution of the two parameters suggests that the width in the Wide condition is proportional to the width in the Narrow condition, with a scaling factor greater than one (Fig. 4a,b). We thus fit a model in which for each participant a scaling relationship is enforced between the widths of all the voxels in the two conditions, i.e., $\sigma_w = r_\sigma \sigma_n$, where r_σ is a participant-specific scaling parameter. We find that this scaling parameter is significantly greater than 1 (t-test $t(38) = 7.72, P = 2.7 \times 10^{-9}$), and, as hypothesized, significantly lower than 2 ($t(38) = 17.6, P = 7 \times 10^{-20}$). Its across-participant average is 1.3 (also its median), and its standard deviation is 0.22 (Fig. 4e). This relatively low dispersion suggests that the same underlying mechanism operates across participants, and prompts us to examine a 'fixed scaling' model in which all the participants have the same scaling factor (chosen equal to the median factor in the model just presented, i.e., $r_\sigma = 1.3$). This yields a significantly better fit than with participant-specific scaling factors ($t(38) = 5.08, P = 10^{-5}$), than with free width parameters for all the voxels across the two conditions ($t(38) = 10.5, P = 9 \times 10^{-13}$), and than with equal widths across conditions ($\sigma_n = \sigma_w; t(38) = 5.06, P = 10^{-5}$; Fig. 4f). Thus a better and more parsimonious account of the data is obtained by assuming that from the Narrow to the Wide condition the widths of the receptive fields scale up by the same factor for all the participants.

This is our best-fitting model of the fMRI data. It is a highly constrained model, which enforces a linear relationship with a specific slope, 2, between the preferred numerosities across conditions, i.e., $\mu_w = 10 + 2(\mu_n - 10)$, for $\mu_n \geq 10$, and a linear scaling of the receptive-field widths across conditions, i.e., $\sigma_w = r_\sigma \sigma_n$, with $r_\sigma > 1$. We have also examined the amplitudes, and found no evidence that they change across conditions (see Supplementary Information).

Less precise neural coding with the wider prior

We have documented substantial changes in the tuning properties of numerosity-sensitive neural populations in the right parietal cortex, across the two conditions (Figs. 2,3,4). These individual tuning adjustments, taken together, are likely to affect the overall acuity of the

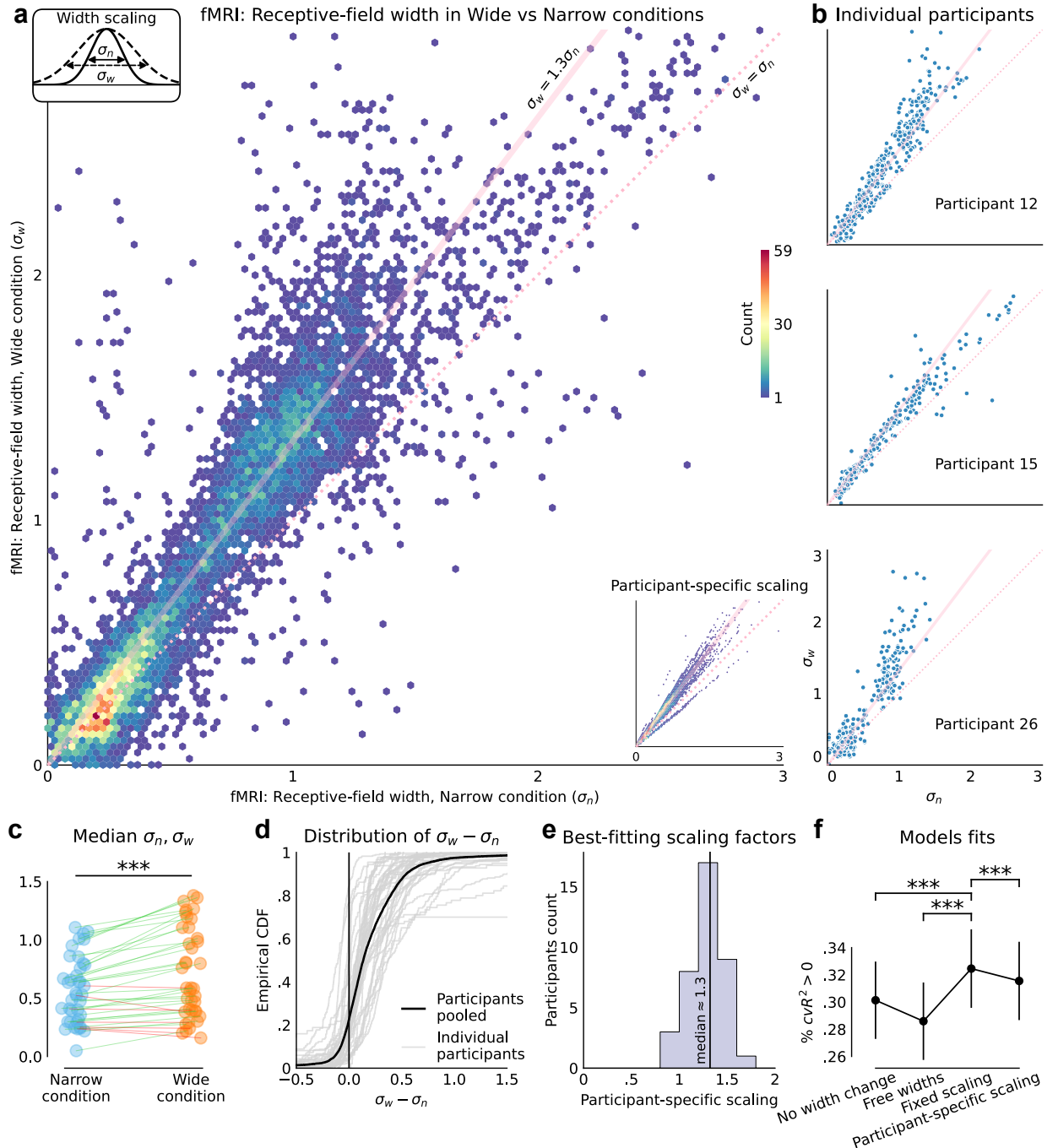


Fig. 4: The receptive fields broaden under the wider range. **a**, Distribution of the voxels' pairs of best-fitting widths parameters (σ_n , σ_w) in the Wide vs. Narrow conditions (participants pooled, 'free-widths' model). The widths in the Wide condition are approximately proportional to those in the Narrow condition, with a ratio greater than 1, indicating a widening of the receptive fields (transparent pink line: ratio 1.3, dotted pink line: identity function). 2.44% of outlier voxels not shown because one width is outside the figure range. Inset: Same distribution, with the 'participant-specific scaling' model. **b**, Widths in the Wide vs. Narrow conditions for three representative participants ('free-widths' model). Pink lines as in **a**. (caption continued on next page)

Fig. 4: (cont.) **c**, Median widths for each participant in the Narrow (left) and Wide (right) conditions. A green (resp., red) line indicates that the participant’s median width in the Wide condition is greater (resp., lower) than in the Narrow condition. **d**, Empirical cumulative distribution of the difference between each voxel’s widths in the Wide and Narrow condition, $\sigma_w - \sigma_n$, for each participant (gray lines) and for the participants pooled (black line). For a majority of voxels this difference is positive, i.e., most voxels’ receptive fields widen in the Wide condition. **e**, Distribution of the width-scaling parameter across participants (‘participant-specific scaling’ model). **f**, Across-participants average of the proportion of voxels with positive cross-validated variance explained ($cvR^2 > 0$) for (from left to right) the model with no change in the voxels’ widths parameters, the model with free width parameters (shown in **a**), the ‘fixed width-scaling’ model, and the model with participant-specific scalings (inset of **a**), all with the efficient-shift relation on the preferred numerosities. The ‘fixed width-scaling’ model outperforms the other three. Error bars show ± 1 standard error of the mean. ***: $P < 0.001$.

neural code. Specifically, in the Wide condition, receptive fields are more spread out and broader, a pattern that presumably reduces encoding precision, consistent with a dynamic implementation of efficient coding. We now test this by estimating the imprecision of the neural code, in the two conditions.

We derive a measure of the encoding precision from the parameters of our nPRF model, combined with a noise component that we estimate by fitting a multivariate distribution to the residuals of the model⁴⁸ (see [Methods](#)). We estimate the encoding Fisher information⁴⁹, a statistical measure of precision, for each participant and condition. We find that the inverse of its square-root, $1/\sqrt{I}$ (a lower bound on the standard deviation of estimates), is significantly larger in the Wide condition than in the Narrow condition (one-sided paired t-test: $t(38) = 6.53, P = 5 \times 10^{-8}$; Fig. 5a, left panel), indicating reduced precision of neural encoding in the Wide condition. We note, however, that the Fisher information measures sensitivity to infinitesimal changes in the stimulus, and is mostly relevant in the small-noise regime of unbiased estimators of continuous quantities.

Thus, to better quantify the precision of the neural encoding, we adopt a simulation-based approach by which we measure the expected variability of estimates decoded from simulated neural activity. Specifically, we generate noisy neural responses from the encoding model, and decode them into number estimates, by taking the posterior mean. We obtain distributions of such simulated fMRI-derived numerosity estimates, by repeating this procedure 20,000 times for each participant, numerosity, and condition (see also [Methods](#)). The mean absolute error of these simulated decoded estimates is significantly larger in the Wide condition than in the Narrow condition (one-sided paired t-test: $t(38) = 3.48, P = 6 \times 10^{-4}$; Fig. 5a, right panel), consistent with the Fisher-information analysis above. Moreover, the standard deviation of the fMRI-derived numerosity estimates as a function of the true numerosities mirrors the pattern of participants’ behavioral variability (compare Fig. 5b to Fig. 1b), with consistently higher variability in the Wide condition.

As a control analysis, we also decode neural responses from the Narrow condition using the Wide prior. This manipulation only modestly increases the variability relative

to the Narrow prior, with the main difference being the absence of a boundary effect at 25 (Fig. 5b, dashed line). This result indicates that the increased variability in the Wide condition is primarily driven by changes in neural encoding, rather than by the decoding prior.

Changes in neural coding correlate with changes in behavioral variability

The fMRI data suggest decreased precision of the neural representations of numbers in the Wide condition (Fig. 5a,b), and the behavioral data exhibit an increase of the participants' response variability (Fig. 1b). Both findings are consistent with dynamic efficient coding, i.e., a reallocation of representational resources when the range widens, leading to less precise encoding. We now link our behavioral and neural results, and investigate whether the changes in neural coding precision seem to drive the observed increase in behavioral variability. Specifically, we examine whether the statistics of the fMRI-derived numerosity estimates are predictive of those of the participants' estimates.

Prior studies have shown that participants with less precise tuning in right IPS are more imprecise in binary choices involving numbers^{44,45,50}. Consistent with these findings (but here with an estimation task), we find that the standard deviations of behavioral estimates and of fMRI-derived estimates are significantly correlated across participants, in both conditions (Narrow: Pearson's $r = 0.48$, one-sided $P = 0.0011$, $N = 39$; Wide: $r = 0.33$, $P = 0.019$, $N = 39$; Fig. 5c). In short, less precise neural encoding correlates with less precise behavioral responses.

Turning to the question of adaptation, i.e., to the change in encoding across conditions, we first note that participants exhibit individual differences in the degree to which their neural encoding precision adjusts across priors. To capture these differences, we fit a 'participant-specific-slope-and-scaling' model with two parameters: a slope parameter, r_μ , governing shifts in preferred numerosities (i.e., $\mu_w = 10 + r_\mu(\mu_n - 10)$ if $\mu_n \geq 10$, otherwise $\mu_w = \mu_n$), and a width-scaling parameter, r_σ , characterizing changes in tuning width (i.e., $\sigma_w = r_\sigma\sigma_n$). With this model, we ask whether individual variations in neural adaptation predict individual variations in behavioral adaptation. We thus examine the difference across conditions of the standard deviation of responses ($\text{StdDev}_{\text{Wide}} - \text{StdDev}_{\text{Narrow}}$). The difference computed with the behavioral estimates is significantly correlated with the difference computed with the fMRI-derived estimates (Fig. 5d; Pearson's $r = 0.35$, one-sided $P = 0.016$, $N = 38$, excluding one outlier whose behavioral difference is 5 standard deviations from the group mean; including the outlier: $r = 0.23$, $P = 0.079$, $N = 39$, and Spearman's $r = 0.34$, $P = 0.018$, $N = 39$). Thus participants whose neural populations show larger losses of precision with the Wide prior also show greater increases in behavioral variability. Figure 5e,f illustrates for four representative participants how the behavioral changes in variability parallels the fMRI-derived changes in variability.

Neural and behavioral imprecision across numbers

Finally, participants also differ in how their precision varies across numbers. Number representations are roughly consistent with a logarithmic compression, but there are individual variations^{51,52}. Our data allow us to test whether such individual differences

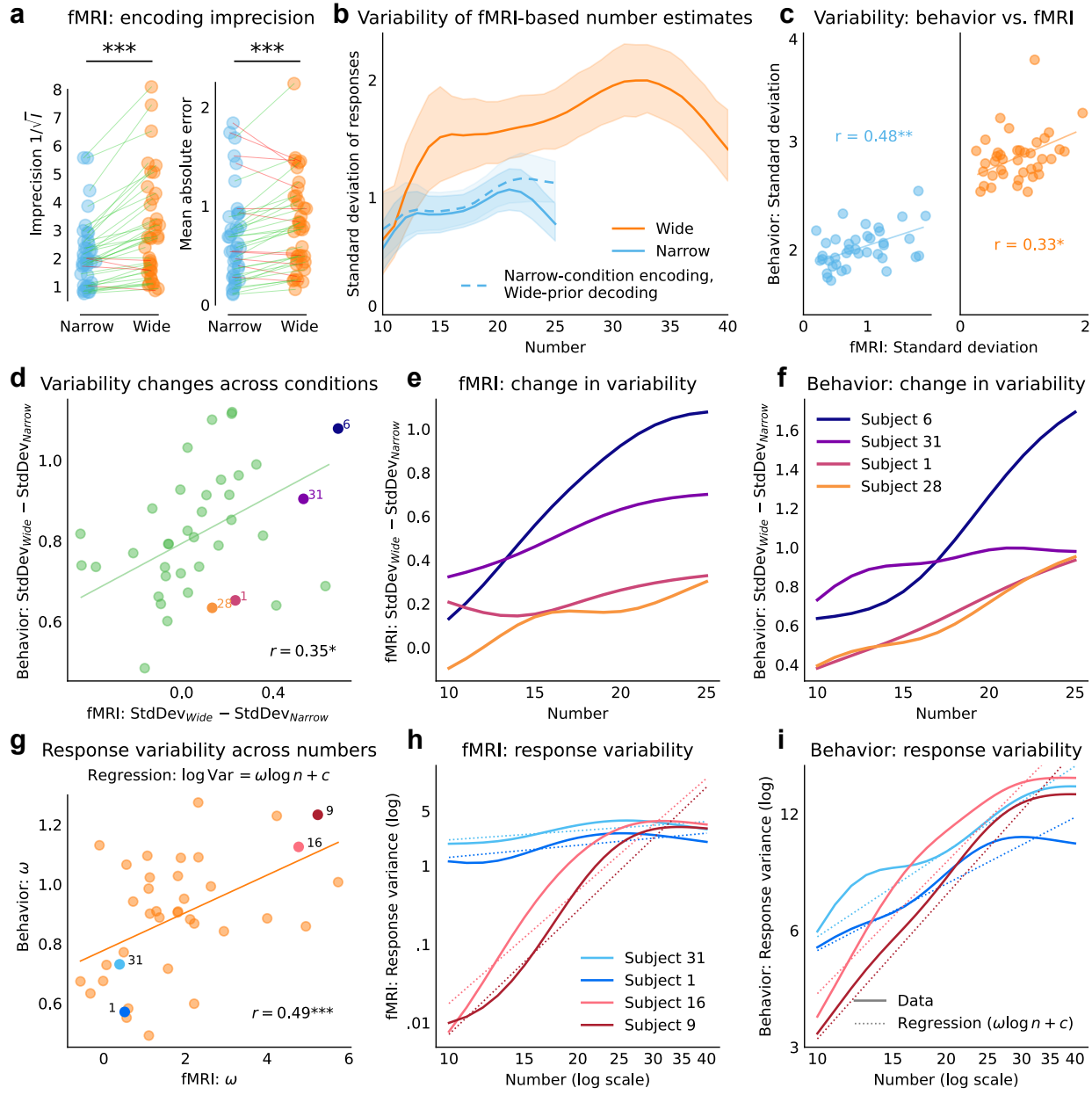


Fig. 5: The neural-code imprecision predicts the behavioral imprecision. **a, Left:** fMRI-derived neural imprecision, measured as the inverse of the square-root of the encoding Fisher information, for each participant in each condition. **Right:** Mean absolute error of fMRI-derived estimates. In both cases, a green (resp., red) line indicates an increase of the quantity (resp., a decrease) in the Wide condition. **b**, Standard deviation of fMRI-derived numerosity estimates, based on the best-fitting nPRF encoding models in each condition, and on the prior in each condition (solid lines), or on the Wide prior (dashed line), as a function of the presented number. Shaded areas show the 95% confidence intervals. **c**, Standard deviation of the numerosity estimates provided by the participants vs. derived from fMRI data, in the Narrow (left) and Wide (right) conditions (in each panel, one point corresponds to one participant).

Fig. 5: (cont.) **d,e,f**, Analysis of the change in imprecision across conditions: **d**, Across-conditions difference in the standard deviation of estimates, as measured in the behavioral data vs. as derived from the fMRI data. A larger increase in fMRI-derived response variability predicts a larger increase in behavioral response variability. **e,f**, Across-conditions difference in the standard deviation of estimates as a function of the presented number, as derived from the fMRI data (**e**) and from the behavioral data (**f**), for four participants that show a diversity of adaptation profiles across numbers. The four participants are shown in **d** with matching colors. **g,h,i**, Analysis of the imprecision varying across numbers: **g**, Parameter ω governing each participant's degree of compression across numbers in the Wide condition (see regression), estimated from the behavioral data vs. from the fMRI data. **h,i**, Response variance (log scale) as a function of the presented number (solid lines), as derived from the fMRI data (**h**) and from the behavioral data (**i**), for four participants that show a diversity of compression across numbers, and corresponding regression lines (dashed lines). The four participants are shown in **g** with matching colors. Individual data in **e,f,h,i** were smoothed with Gaussian kernels of widths 0.2 (**e,g**; log scale) and 3 (**h,i**) to emphasize trend. ***: $P < 0.001$, **: $P < 0.01$, *: $P < 0.05$.

are reflected in parietal tuning profiles. We quantify the compression in both neural and behavioral data by fitting a power law relating response variance (Var) and numerosity (n), as $\log \text{Var} = \omega \log n + c$. This relationship, which can be understood as a generalization of Weber's law (obtained with $\omega = 2$), provides good fits to both behavioral (mean $R^2 = 0.57$, IQR: 0.50-0.68) and fMRI-derived estimates (mean $R^2 = 0.47$, IQR: 0.21-0.74). Here we focus our analysis on the Wide condition, as it encompasses a broader range of numerosities.

Behavioral and neural estimates of ω are significantly correlated (Fig. 5g; $r = 0.49$, one-sided $P = 9.2 \times 10^{-4}$, $N = 38$, excluding one outlier whose behavioral ω is 4.7 standard deviations from the group mean; including the outlier: $r = 0.38$, $P = 0.009$, $N = 39$). Thus, participants whose neural populations show steeper increases in encoding imprecision across numerosities also exhibit stronger behavioral compression (Fig. 5h,i).

Discussion

We have shown that numerosity-sensitive populations in human parietal cortex adapt their tuning to the contextual statistics of numerical stimuli. The encoding precision decreases under the wider prior, consistent with a dynamic implementation of efficient coding. The observed adjustments in preferred numerosities and receptive-field widths follow a predictable pattern, supporting the proposal of distributed range adaptation, whereby populations encode stable quantiles across contexts. Moreover, individual differences in these neural adjustments correlate with individual differences in response variability, suggesting that the observed neural activity underlies behavior. In short, the scaling of the prior prompts the scaling of the neural encoding, which in turn underlies the scaling of the behavioral variability.

Our study extends efficient coding in several ways. First, we show that it applies beyond the perception of physical quantities to abstract magnitudes such as numerosity. Second,

we show that it is a dynamic process which flexibly adapts to changing statistical contexts. Third, we uncover a neural mechanism, distributed range adaptation, through which tuning properties adjust to optimize encoding for the input distribution.

Concretely, distributed range adaptation puts a mathematical constraint on the neural populations' preferred numerosities that one should observe across priors, by requiring their distribution to scale by the same factor as the prior (here, 2). This constraint greatly reduces the flexibility of the population-receptive-fields model, yet it yields a more robust fit than when unconstrained (as evidenced by the increased cross-validated variance explained), indicating that the constraint captures a structuring property of the neural data. Similarly, the receptive-fields widths are well captured by a scaling relation, whereby the wider prior results in wider receptive fields. The best account of the data is obtained by assuming that all the participants shift their preferred numerosities by the same factor, and scale their receptive-field widths by the same factor. This homogeneity further substantiates our conclusions, and suggests that distributed range adaptation is a standard computational mechanism, that structures how sensory networks reorganize in adaptation to changing contexts.

Individual variations nevertheless remain, and enable us to tie participants' behavior to their neural activity. Our results support but also go beyond the finding that participants with less precise neural encoding are also less precise in behavior^{44,45,50}. We show that a participant who adjusts their neural tuning to a greater extent across priors than the average participant, also exhibits larger changes in behavioral variability. Similarly, participants whose neural encoding suggests a stronger compression of larger numbers, also exhibit stronger diminishing sensitivity for larger numerosities, supporting the hypothesis that Weber's law originates in the tuning properties of parietal neurons⁷. In other words, whether we look at variations across conditions or variations across numbers, we find that the precision of the neural encoding is invariably associated with the precision of the behavior, suggesting that the former drives the latter.

Across priors, the widths of the receptive fields scale by a factor smaller than that applied to the prior (1.3 vs. 2). This implies that, relative to the size of the prior, the specificity of the encoding populations is higher with the Wide prior. This is consistent with a recent efficient-coding model of endogenous precision, which predicts that wider priors should result in lower absolute precision but higher relative precision, so as to mitigate the larger errors incurred under the wider priors³⁸.

Our findings were made possible by a combination of methodological choices: we study a relatively large sample of participants (39; with two sessions each), performing an estimation task instead of a (more typical) binary-choice task, and we make extensive use of advanced encoding models of fMRI data, namely, numerical population receptive fields models, to formally quantify the acuity of the neural code. This enables us to effectively test the neural data against targeted hypotheses, and to measure with precision the attributes of the neural substrates that support human representations. This approach also paves the way to elucidating how the acuity of the neural code across stimulus space shapes perceptual biases and, ultimately, decision-making^{30,44–46}.

The notion of distributed range adaptation seems to partially extend to the encoding of spatial location. When a rat's environment is expanded, about 36% of its recorded hippocampal place cells exhibit a corresponding rescaling of the locations of their receptive

fields, such that they code for the same relative position across environments, consistent with a 2D extension of our results^{53,54}. Notably, the areas of the receptive fields of these place cells moreover increase with the area of the environment, but they scale by a ratio smaller than the scaling factor applied to the environment, analogous to our results regarding the receptive-fields widths, and pointing to a similar mechanism⁵³.

Distributed range adaptation requires encoding populations to update their tuning properties, and to do so in a mutually consistent manner, to maintain a coherent collective code. We note in addition that behavioral evidence suggests that this adaptation may occur relatively fast (on the order of a second³⁹). Changes in neuronal tuning could be implemented via synaptic reweighting^{55,56}, or via gain adaptation in a recurrent network^{39,57}. Network updates could be driven by top-down modulatory signals, or by local learning rules implementing quantile regression⁵⁸, as in recent models of distributional reinforcement learning^{59,60}.

References

1. Hubel, D. H. & Wiesel, T. N. Receptive Fields of Single Neurones in the Cat's Striate Cortex. *The Journal of Physiology* **148**, 574–591. issn: 00223751 (Oct. 1959).
2. Joseph, A. Discharge Patterns of Single Fibers in the Cat's Auditory Nerve. *Journal of Communication Disorders* **1**, 104–105. issn: 00219924 (May 1967).
3. Dubner, R. & Zeki, S. Response Properties and Receptive Fields of Cells in an Anatomically Defined Region of the Superior Temporal Sulcus in the Monkey. *Brain Research* **35**, 528–532. issn: 00068993 (Dec. 1971).
4. Maffei, L. & Fiorentini, A. The Visual Cortex as a Spatial Frequency Analyser. *Vision Research* **13**, 1255–1267. issn: 00426989 (July 1973).
5. Simons, D. J. Response Properties of Vibrissa Units in Rat SI Somatosensory Neocortex. *Journal of Neurophysiology* **41**, 798–820. issn: 0022-3077, 1522-1598 (May 1978).
6. Nieder, A., Freedman, D. J. & Miller, E. K. Representation of the Quantity of Visual Items in the Primate Prefrontal Cortex. *Science* **297**, 1708–1711. issn: 0036-8075, 1095-9203 (Sept. 2002).
7. Tsouli, A. *et al.* The Role of Neural Tuning in Quantity Perception. *Trends in Cognitive Sciences* **26**, 11–24. issn: 13646613 (Jan. 2022).
8. Brunel, N. & Nadal, J. P. Mutual Information, Fisher Information, and Population Coding. *Neural computation* **10**, 1731–57. issn: 0899-7667. PMID: 9744895 (1998).
9. Ma, W. J., Beck, J. M., Latham, P. E. & Pouget, A. Bayesian inference with probabilistic population codes. *Nature Neuroscience* **9**, 1432–1438. issn: 1097-6256 (2006).
10. Attneave, F. Some informational aspects of visual perception. *Psychological Review* **61**, 183–193. issn: 0033-295X (1954).
11. Barlow, H. B. in *Sensory Communication* 216–234 (1961). isbn: 9780262518420.
12. Ganguli, D. & Simoncelli, E. P. Efficient Sensory Encoding and Bayesian Inference with Heterogeneous Neural Populations. *Neural Computation* **26**, 2103–2134. issn: 0899-7667 (Oct. 2014).
13. Prat-Carrabin, A. & Woodford, M. *Bias and Variance of the Bayesian-mean Decoder in Advances in Neural Information Processing Systems* (eds Ranzato, M., Beygelzimer, A., Dauphin, Y., Liang, P. S. & Vaughan, J. W.) **34** (Curran Associates, Inc., 2021), 23793–23805.
14. Laughlin, S. A simple coding procedure enhances a neuron's information capacity. *Zeitschrift für Naturforschung. Section C: Biosciences* **36**, 910–2. issn: 0341-0382 (1981).

15. Olshausen, B. A. & Field, D. J. Emergence of simple-cell receptive field properties by learning a sparse code for natural images. *Nature* **381**, 607–609. issn: 0028-0836 (1996).
16. Brenner, N., Bialek, W. & de Ruyter van Steveninck, R. Adaptive Rescaling Maximizes Information Transmission. *Neuron* **26**, 695–702. issn: 08966273 (June 2000).
17. Fairhall, A. L., Lewen, G. D., Bialek, W. & de Ruyter van Steveninck, R. R. Efficiency and ambiguity in an adaptive neural code. *Nature* **412**. Publisher: Nature Publishing Group, 787–792. issn: 1476-4687 (Aug. 2001).
18. Tobler, P. N., Fiorillo, C. D. & Schultz, W. Adaptive coding of reward value by dopamine neurons. *Science (New York, N.Y.)* **307**, 1642–1645. issn: 1095-9203 (Mar. 2005).
19. Padoa-Schioppa, C. Range-Adapting Representation of Economic Value in the Orbitofrontal Cortex. *The Journal of Neuroscience* **29**, 14004–14014. issn: 0270-6474 (2009).
20. Womelsdorf, T., Anton-Erxleben, K., Pieper, F. & Treue, S. Dynamic shifts of visual receptive fields in cortical area MT by spatial attention. *Nature Neuroscience* **9**, 1156–1160. issn: 1097-6256 (2006).
21. Klein, B. P., Harvey, B. M. & Dumoulin, S. O. Attraction of Position Preference by Spatial Attention throughout Human Visual Cortex. *Neuron* **84**, 227–237. issn: 0896-6273 (2014).
22. Dragoi, V., Sharma, J. & Sur, M. Adaptation-Induced Plasticity of Orientation Tuning in Adult Visual Cortex. *Neuron* **28**. Publisher: Elsevier, 287–298. issn: 0896-6273 (Oct. 2000).
23. Dragoi, V., Sharma, J., Miller, E. K. & Sur, M. Dynamics of neuronal sensitivity in visual cortex and local feature discrimination. *Nature Neuroscience* **5**. Publisher: Nature Publishing Group, 883–891. issn: 1546-1726 (Sept. 2002).
24. Tsouli, A. *et al.* Adaptation to Visual Numerosity Changes Neural Numerosity Selectivity. *NeuroImage* **229**, 117794. issn: 1053-8119 (Apr. 2021).
25. Mello, G. B. M., Soares, S. & Paton, J. J. A Scalable Population Code for Time in the Striatum. *Current Biology* **25**, 1113–1122. issn: 0960-9822 (May 2015).
26. Shimbo, A., Izawa, E. I. & Fujisawa, S. Scalable Representation of Time in the Hippocampus. *Science Advances* **7**. issn: 23752548 (2021).
27. Walsh, V. A theory of magnitude: common cortical metrics of time, space and quantity. *Trends in Cognitive Sciences* **7**, 483–488. issn: 1364-6613 (2003).
28. Kable, J. W. & Glimcher, P. W. The Neural Correlates of Subjective Value during Intertemporal Choice. *Nature Neuroscience* **10**, 1625–1633. issn: 1546-1726 (Dec. 2007).
29. Fehr, E. & Camerer, C. F. Social Neuroeconomics: The Neural Circuitry of Social Preferences. *Trends in Cognitive Sciences* **11**, 419–427. issn: 1364-6613, 1879-307X (Oct. 2007).
30. Woodford, M. Modeling Imprecision in Perception, Valuation, and Choice. *Annual Review of Economics* **12**, 1–23. issn: 1941-1383 (2020).
31. Dehaene, S. *The number sense: How the mind creates mathematics* (Oxford University Press, 2011).
32. Nieder, A. The Evolutionary History of Brains for Numbers. *Trends in Cognitive Sciences*. issn: 1364-6613 (2021).
33. Nieder, A. The neuronal code for number. *Nature Reviews Neuroscience* **17**, 366–382. issn: 1471-003X (2016).
34. Nieder, A. & Miller, E. K. Coding of Cognitive Magnitude Compressed Scaling of Numerical Information in the Primate Prefrontal Cortex. *Neuron* **37**, 149–157. issn: 0896-6273 (2003).
35. Harvey, B. M., Klein, B. P., Petridou, N. & Dumoulin, S. O. Topographic Representation of Numerosity in the Human Parietal Cortex. *Science* **341**, 1123–1126. issn: 0036-8075 (2013).
36. Kutter, E. F., Bostroem, J., Elger, C. E., Mormann, F. & Nieder, A. Single Neurons in the Human Brain Encode Numbers. *Neuron* **100**, 753–761.e4. issn: 0896-6273 (2018).

37. Kutter, E. F. *et al.* Single-Neuron Representation of Nonsymbolic and Symbolic Number Zero in the Human Medial Temporal Lobe. *Current Biology* **34**, 4794–4802.e3. ISSN: 0960-9822 (Oct. 2024).
38. Prat-Carrabin, A. & Woodford, M. Endogenous Precision of the Number Sense. *eLife (Reviewed Preprint)* (2024).
39. Prat-Carrabin, A., Harl, M. V. & Gershman, S. J. *Fast Efficient Coding and Sensory Adaptation in Gain-Adaptive Recurrent Networks* July 2025.
40. Frydman, C. & Jin, L. J. Efficient Coding and Risky Choice. *The Quarterly Journal of Economics* **137**, 161–213. ISSN: 0033-5533 (Dec. 2021).
41. Prat-Carrabin, A. & Woodford, M. Efficient coding of numbers explains decision bias and noise. *Nature Human Behaviour* **6**, 1142–1152 (2022).
42. Cai, Y. *et al.* Topographic Numerosity Maps Cover Subitizing and Estimation Ranges. *Nature Communications* **12**, 3374. ISSN: 2041-1723 (June 2021).
43. Harvey, B. M. & Dumoulin, S. O. A Network of Topographic Numerosity Maps in Human Association Cortex. *Nature Human Behaviour* **1**, 0036. ISSN: 2397-3374 (Jan. 2017).
44. Barreto-García, M. *et al.* Individual risk attitudes arise from noise in neurocognitive magnitude representations. *Nature Human Behaviour* **7**, 1551–1567 (2023).
45. de Hollander, Gilles, Grueschow, M., Hennel, F. & Ruff, C. C. *Rapid Changes in Risk Preferences Originate from Bayesian Inference on Parietal Magnitude Representations* Aug. 2024.
46. de Hollander, Gilles, Moisa, M. & Ruff, C. C. *Risk Preferences Causally Rely on Parietal Magnitude Representations: Evidence from Combined TMS-fMRI* Jan. 2025.
47. Aqil, M., Knapen, T. & Dumoulin, S. O. Divisive normalization unifies disparate response signatures throughout the human visual hierarchy. *Proceedings of the National Academy of Sciences* **118**, e2108713118. ISSN: 0027-8424 (2021).
48. Van Bergen, R. S., Ma, W. J., Pratte, M. S. & Jehee, J. F. M. Sensory uncertainty decoded from visual cortex predicts behavior. *Nature Neuroscience* **18**, 1728. ISSN: 1097-6256 (2015).
49. Zhang, L.-Q., Mao, J., Aguirre, G. K. & Stocker, A. A. The tilt illusion arises from an efficient reallocation of neural coding resources at the contextual boundary. *Proceedings of the National Academy of Sciences* **122**, e2421565122. ISSN: 0027-8424 (2025).
50. Lasne, G., Piazza, M., Dehaene, S., Kleinschmidt, A. & Eger, E. Discriminability of numerosity-evoked fMRI activity patterns in human intra-parietal cortex reflects behavioral numerical acuity. *Cortex* **114**, 90–101. ISSN: 0010-9452 (2019).
51. Feigenson, L., Dehaene, S. & Spelke, E. Core systems of number. *Trends in Cognitive Sciences* **8**, 307–314. ISSN: 1364-6613 (2004).
52. Lourenco, S. F. & Longo, M. R. Multiple spatial representations of number: evidence for co-existing compressive and linear scales. *Experimental Brain Research* **193**, 151–156. ISSN: 0014-4819 (2009).
53. Muller, R. U. & Kubie, J. L. The Effects of Changes in the Environment on the Spatial Firing of Hippocampal Complex-Spike Cells. *Journal of Neuroscience* **7**, 1951–1968. ISSN: 0270-6474, 1529-2401 (July 1987).
54. O’Keefe, J. & Burgess, N. Geometric Determinants of the Place Fields of Hippocampal Neurons. *Nature* **381**, 425–428. ISSN: 1476-4687 (May 1996).
55. Abbott, L. F., Varela, J. A., Sen, K. & Nelson, S. B. Synaptic Depression and Cortical Gain Control. *Science* **275**, 221–224 (Jan. 1997).
56. Westrick, Z. M., Heeger, D. J. & Landy, M. S. Pattern Adaptation and Normalization Reweighting. *Journal of Neuroscience* **36**, 9805–9816. ISSN: 0270-6474, 1529-2401 (Sept. 2016).
57. Duong, L. R., Bredenberg, C., Heeger, D. J. & Simoncelli, E. P. Adaptive Coding Efficiency in Recurrent Cortical Circuits via Gain Control. *arXiv: 2305.19869* (2023).

58. Jain, R. & Chlamtac, I. The P2 Algorithm for Dynamic Calculation of Quantiles and Histograms without Storing Observations. *Commun. ACM* **28**, 1076–1085. issn: 0001-0782 (Oct. 1985).
59. Dabney, W., Rowland, M., Bellemare, M. G. & Munos, R. Distributional Reinforcement Learning with Quantile Regression. *32nd AAAI Conference on Artificial Intelligence, AAAI 2018*, 2892–2901. issn: 2159-5399. arXiv: [1710.10044](https://arxiv.org/abs/1710.10044) (2018).
60. Lowet, A. S., Zheng, Q., Matias, S., Drugowitsch, J. & Uchida, N. Distributional Reinforcement Learning in the Brain. *Trends in Neurosciences* **43**, 980–997. issn: 1878108X (2020).

Methods

Task and participants

Thirty-nine healthy participants (13 females, aged 18-34, mean age 23.1) participated in the experiment. Participants were provided information about the objective of the study, the equipment used, the data recorded, the task, as well as the payoff mechanism. Participants were screened for MR compatibility. No participant showed indications of psychiatric or neurological disorders or needed visual correction. The experiment conformed to the Declaration of Helsinki and was approved by the Canton of Zurich's Ethics Committee. All the participants provided their written consent after being presented with the relevant information.

Each participant completed two experimental sessions, each lasting approximately one hour, with an additional 45 minutes for preparatory procedures such as changing into scanning attire and scanner setup. Each session included two blocks corresponding to the Narrow and Wide conditions, presented in pseudo-random, counterbalanced order.

Each block started with a *learning phase* (15 trials). In each trial of this phase, the participant was shown a stimulus together with its objective numerosity, represented by an Arabic numeral. The participant could progress from one trial to the next at their own pace, and no further response was asked of them in this phase.

The *learning phase* was followed by the *feedback phase* (30 trials), during which participants estimated the numerosity of the presented stimulus and received feedback on the ground truth numerosity after each response. Each trial in this phase began with a green fixation cross (300 ms), followed by a red fixation cross (300 ms), and then the presentation of the stimulus array within a 2.5° visual angle aperture (600 ms). Immediately after the stimulus, a slider appeared, scaled proportionally to the current prior range. Participants used an MRI-compatible trackball to indicate their perceived numerosity, with no time limit for their response. After response submission, the correct numerosity was displayed as feedback for 500 ms. The *learning* and *feedback phases* aimed to familiarize participants with the stimuli and the prior distribution of the current condition.

After the *learning* and *feedback phases*, participants performed the *main task* (see Fig. 1a). Each trial in the *main task* started with a green fixation cross (300 ms), followed by a red fixation cross (300 ms), and then the stimulus array, which was presented for 600 ms. Crucially, a variable delay of 4, 5, or 6 seconds (randomly selected) followed the stimulus, during which only a white fixation cross was displayed. This temporal separation ensured that stimulus-related BOLD activity was not contaminated by decision-making and motor response-related BOLD activity^{61–63}. In the main task, participants were given three seconds

to provide their estimate. Each block of the main task comprised 120 trials (4 runs of 30 trials). Thus, each session included 240 trials, and a total of 480 trials were collected per participant (240 trials per condition).

At the end of the experiment, participants received a reward consisting of a participation fee (30 CHF/hour) plus a performance bonus. The performance bonus was calculated based on estimate accuracy: for each trial, an amount equal to $\text{CHF } 0.07 - (\hat{x} - x)^2 / 600$ was added to the bonus, where \hat{x} is the participant's estimate and x is the ground truth numerosity. Trials from both the *main task* and the *feedback*-phase contributed to the performance bonus. Late responses incurred a penalty of CHF 0.10 per trial, deducted from the bonus. All participants earned a positive performance bonus, with an average of CHF 29.77 (sd: CHF 6.00) across the two sessions (CHF 1 \approx USD 1.25 at current exchange rates).

MRI data acquisition

We acquired structural and functional MRI data using a Philips (Best, the Netherlands) Achieva 3T whole-body MR scanner equipped with a 32-channel MR head coil, located at the Laboratory for Social and Neural Systems Research (SNS-Lab) of the UZH Zurich Center for Neuroeconomics. In both sessions, we collected 8 runs of fMRI data with a T2*-weighted gradient-recalled echo-planar imaging (GR-EPI) sequence (132 volumes + 5 dummies; flip angle 90 degrees; TR = 2286 ms, TE = 30ms; matrix size 96×70 , FOV $240 \times 175\text{mm}$; in-plane resolution of 2.5 mm; 39 slices with thickness of 2.5 mm and a slice gap of 0.5mm; SENSE acceleration in phase-encoding direction (left-right) with factor 1.5; time-of-acquisition 5:02 minutes). At the beginning of each session, we acquired high-resolution T1-weighted 3D MPRAGE image (FOV: $256 \times 256 \times 170$ mm; resolution 1 mm isotropic; Shot TR = 2800 ms; TI = 1098.6 ms; 256 shots, flip angle 8 degrees; TR = 8.3 ms; TE = 3.9 ms; SENSE acceleration in left-right direction 2; time-of-acquisition 5:35 minutes), while participants performed the *learning* and *feedback* phases.

MRI preprocessing

Preprocessing of fMRI data was performed using *fMRIprep* 23.2.1^{64,65}, which is based on *Nipype* 1.8.6^{66,67}.

Preprocessing of B0 inhomogeneity mappings

A *B0*-nonuniformity map (or *fieldmap*) was estimated based on two or more echo-planar imaging (EPI) references using *topup*⁶⁸ (FSL).

Anatomical data preprocessing

Each T1w image was corrected for intensity non-uniformity (INU) using *N4BiasFieldCorrection*⁶⁹, distributed with ANTs 2.5.0. The T1w reference was then skull-stripped using a *Nipype* implementation of the *antsBrainExtraction.sh* workflow (ANTs), with OASIS30ANTs as the target template. Brain tissue segmentation of cerebrospinal fluid (CSF), white matter

(WM), and gray matter (GM) was performed on the brain-extracted T1w using `fast`⁷⁰ (FSL). An anatomical T1w-reference map was computed after registration of the 4 INU-corrected T1w images using `mri_robust_template`⁷¹ (FreeSurfer 7.3.2). Brain surfaces were reconstructed using `recon-all`⁷² (FreeSurfer 7.3.2). The brain mask estimated previously was refined using a custom variation of the method to reconcile ANTs-derived and FreeSurfer-derived segmentations of the cortical gray matter⁷³. Volume-based spatial normalization to the MNI152NLin2009cAsym standard space was performed through non-linear registration with `antsRegistration` (ANTs 2.5.0), using brain-extracted versions of both the T1w reference and the T1w template. The following template was selected for spatial normalization and accessed via *TemplateFlow*⁷⁴ (version 23.1.0): *ICBM 152 Nonlinear Asymmetrical template version 2009c*⁷⁵ (TemplateFlow ID: MNI152NLin2009cAsym).

Functional data preprocessing

For each of the 16 BOLD runs per participant (across all tasks and sessions), the following preprocessing steps were performed. First, a reference volume was generated using a custom *fMRIPrep* methodology for head-motion correction. Head-motion parameters (transformation matrices and six corresponding rotation and translation parameters) were estimated with respect to the BOLD reference using `mcflirt`⁷⁶ (FSL), prior to any spatiotemporal filtering. The estimated *fieldmap* was aligned to the target EPI reference run using rigid registration, and the field coefficients were mapped onto the reference EPI.

The BOLD reference was co-registered to the T1w reference using `bbregister` (FreeSurfer), which implements boundary-based registration⁷⁷. Co-registration was configured with six degrees of freedom. Several confounding time series were calculated based on the preprocessed BOLD data: framewise displacement (FD), DVARS, and three region-wise global signals (CSF, WM, and whole-brain). FD was computed using two formulations: absolute sum of relative motions⁷⁸ and relative root mean square displacement between affines⁷⁶. FD and DVARS were calculated for each functional run using their *Nipype* implementations⁷⁸. Many internal operations in *fMRIPrep* use *Nilearn* 0.10.2⁷⁹. For further details, see the *fMRIPrep* workflow documentation.

fMRI analysis

The key aim of our fMRI analyses was to estimate the nonlinear tuning of neuronal populations in the parietal cortex to numerosity, and how this tuning was shaped by different task contexts (i.e., priors), following established approaches^{61–63,80}. After preprocessing, the analysis proceeded in three phases:

1. Estimating voxelwise BOLD responses for every trial using a single-trial GLM.
2. Fitting a large set of numerical population receptive field (nPRF) models, differing in complexity and scientific assumptions, and comparing them using cross-validated R^2 .
3. Using statistical measures to quantify the information about numerosity contained in parietal activity, and how this varied with task context and numerosity.

These phases will be described in detail in the following sections.

Single-trial BOLD response estimation

We used the GLMSingle Python package⁸¹ to estimate single-trial BOLD response amplitudes. This package employs cross-validation to optimize a generalized linear model (GLM) by selecting: 1) the most suitable hemodynamic response function from a predefined library, 2) the optimal L2-regularization parameter to mitigate the effects of correlated single-trial regressors, and 3) GLMDenoise regressors⁸², derived from the first n principal components of noise voxels (defined as voxels with low explained variance in the task-based GLM). The number of principal components was determined via cross-validation.

To construct the design matrix for GLMSingle, we modeled the onsets of both (1) the stimulus arrays of different numerosities and (2) the response periods. Trials were categorized for cross-validation as either stimulus trials (e.g., stimulus_10) or response trials (e.g., response_11 or no_response). Based on extensive pilot analyses, as well as earlier studies^{62,63}, we chose not to include additional confound regressors (e.g., motion parameters, RETROICOR, or aCompCor) beyond those provided by GLMDenoise. This decision follows prior work showing that additional regressors often correlate with those derived by GLMDenoise and typically do not further improve decoding accuracy; in fact, they can sometimes reduce it by introducing overfitting^{62,81,82}.

nPRF estimation

To estimate nPRF parameters and test our hypotheses, we fitted a number of numerical population receptive field (nPRF) models. These models only differed in the extent to which parameters were (a) constant over conditions (b) completely free between conditions or (c) a linear function of each other (e.g., $\mu_w = 10 + \beta(\mu_n - 10)$), where β could either be fixed or estimated. All nPRF models describes the average responses of a voxel to different numerosities as a function of the number x , as follows:

$$f(x) = b + a \exp\left(-\frac{(\log x - \log \mu)^2}{2\sigma^2}\right), \quad (1)$$

where b is the baseline, a the amplitude, μ the voxel's preferred numerosity, and σ the width parameter of the receptive field.

The nPRF model fitting started with a grid search, making relative activation predictions for each trial using 41 possible preferred numerosities (5-41) and 30 possible width (2-30 in natural space). For each voxel, the parameters corresponding to the predicted activation profile with the highest correlation with the actual activation profile was chosen, after which the amplitude and baseline parameters were estimated using ordinary least-squares (OLS). After this initial step, parameters were further optimized using the ADAM gradient descent optimisation algorithm⁸³, as implemented in Tensorflow⁸⁴, with the negative relative explained variance (R^2) as a cost function.

Some of the models we used put 'hierarchical' constraints on the parameters using scaling parameters β . For example, the preferred numerosity of a voxel in the Wide condition was a linear function of the numerosity in the Narrow condition with a slope

parameter that is estimated but kept constant across voxels. For these models, the grid search was performed on all voxels, and the mean slope was used as a starting point for the gradient descent optimization.

The nPRF model was fitted both to all voxels within the brain (for visualization purposes), or specifically to voxels in the right NPC. The right NPC mask was taken directly from Barretto-García et al.⁶¹. In the case of models with hierarchical parameters, this latter approach was necessary, since we did not want voxels outside of the ROI to influence the slope parameter β .

For all models, we fitted both a version of the model in which the average BOLD activity is a function of the *actual ground-truth numerosity* at each trial, and a version in which the BOLD response would be a function of the *response provided by the participant*. The variants that uses the responses generally yielded a higher proportion of variance explained cvR^2 (see Supplementary Information). Thus we use these models for the analyses of the voxels' tuning (Figs. 3,4). However, when we related the relative acuity of the neural responses to behavioral differences (Fig. 5), we resorted to the models fitted on the ground-truth numerosities. We did so to make sure the fMRI noise estimates and the behavioral responses were statistically completely independent, and avoid 'double-dipping'.

To identify voxels with reliable numerosity-tuned responses and to facilitate model comparison, we employed an 8-fold cross-validation procedure. For each participant and model, we generated eight distinct train–test splits by iteratively leaving out the n th run from both the first and second sessions. This ensured equal representation of the Narrow and Wide conditions in both the training set (210 out of 420 trials each) and the test set (30 out of 60 trials each). The nPRF model was fitted to the training data, and its performance was evaluated using the explained variance (R^2) on the held-out test trials, yielding a cross-validated R^2 (cvR^2). This procedure enabled us to identify voxels with robust and generalizable numerosity tuning while excluding unreliable or noisy responses⁸⁵. Throughout the manuscript, analyses of pRF parameters are restricted to voxels with an average cvR^2 across test runs greater than 0.0.

For model selection at the voxel level, we compared cross-validated explained variance (cvR^2) across candidate models. For each voxel, the model with the highest average cvR^2 across folds was designated as the best-fitting model. Because cvR^2 is evaluated on independent test data, it penalizes overly complex models that overfit noise in the training set. This makes cvR^2 a principled criterion for voxel-wise model comparison, as it favors models that capture reliable neural response mechanisms rather than spurious or idiosyncratic patterns.

For model selection across voxels (e.g., Fig. 3f), we used the proportion of voxels with $cvR^2 > 0.0$. This approach was motivated by the observation that, in noise voxels, nPRF models tend to overfit and can perform much worse than a simple intercept model, yielding very negative (average) cvR^2 values. Consequently, the distribution of cvR^2 across voxels is highly variable with a heavy negative tail. Using the proportion of voxels with positive cvR^2 provides a more stable and interpretable summary measure for model comparison at the population level.

For visualization, voxelwise nPRF parameters were projected onto the cortical surface using the FreeSurfer surfaces generated by fMRIprep. In particular, we visualized the preferred numerosity of individual vertices. To sample voxelwise pRF parameters onto the

surface, we used Nilearn’s `vol_to_surf` function⁷⁹. Vertices without reliable numerosity tuning were excluded using the $cvR^2 > 0.0$ mask.

All nPRF analyses were implemented using the `braincoder` package⁸⁶, which provides flexible tools for specifying encoding models and estimating them with a GPU-accelerated TensorFlow backend.

fMRI-derived Fisher information

To quantify differences in the acuity with which right NPC represents numerosity across participants, conditions, and numerosities, we used the statistical measure of *Fisher Information*⁸⁷. Fisher Information quantifies the sensitivity of a likelihood function to changes in a parameter θ (in our case, numerosity n), and is defined as

$$I(n) = \mathbb{E} \left[\left(\frac{\partial}{\partial n} \log p(y | n) \right)^2 \right], \quad (2)$$

where $p(y | n)$ denotes the likelihood of observing a BOLD activation pattern y given numerosity n , and the expectation is taken with respect to $p(y | n)$. The inverse of the Fisher Information provides a lower bound on the variance of any unbiased decoder of n (the Cramér–Rao bound). Thus, higher Fisher Information implies greater representational acuity and more precise decoding of numerosity.

Thus, our first step was to define a likelihood function $p(y | n)$, following the approach used in our earlier work on decoding numerosities^{61–63}. The crucial step was to extend the *deterministic* nPRF model,

$$y = f(n; \theta), \quad (3)$$

where $\theta = \{\mu, \sigma, A, b\}$ denotes the preferred numerosity, tuning width, response amplitude, and baseline. This formulation predicts a fixed response pattern for each numerosity, but does not capture trial-to-trial variability in BOLD responses. We therefore extended it into a stochastic model,

$$y = f(n; \theta) + \epsilon, \quad \epsilon \sim \mathcal{N}(0, \Sigma), \quad (4)$$

with the noise term ϵ accounting for variability in the observed responses.

We estimated Σ by fitting a multivariate normal distribution to the residuals of the best-fitting nPRF model^{61–63}, using only signal voxels with $cvR^2 > 0$. While relative covariance in noise across voxels is critical for decoding uncertainty⁸⁸, reliable estimation is extremely challenging in a low- n regime (480 trials) with hundreds of voxels⁸⁹. Although regularized approaches have been proposed⁸⁸, in our initial analyses these performed worse than assuming diagonal (i.e., uncorrelated) noise. In particular, the decoded posteriors were excessively broad and their decoding performance was worse than a model assuming diagonal noise.

Importantly, our aim here was not to decode trial-by-trial uncertainty (as in⁸⁸ and⁶²), but rather to assess how the acuity of numerosity representations varied across participants and conditions. For this purpose, we thus adopted a *diagonal* covariance matrix, assuming no correlations between voxels. Note that these analyses therefore specifically targeted the

effects of the *preferred numerosity* and *width* of numerical pRFs, rather than their noise covariance structure. Notably, preliminary analyses revealed no evidence that noise patterns differed between the Narrow and Wide conditions.

We computed Fisher Information for arbitrary neural encoding models using the `braincoder` package⁸⁶. Since the expectation in Equation 2 cannot readily be expressed in closed form for our models, we evaluated it numerically by sampling from the noise distribution $p(y | n)$. For each sample, we computed the derivative of the log-likelihood with respect to numerosity,

$$\frac{\partial}{\partial n} \log p(y | n),$$

using automatic differentiation. Squaring this term and averaging across samples yields a Monte Carlo estimate of Fisher Information. In practice, we drew 1000 samples for each n , providing a stable numerical evaluation of representational acuity at that numerosity. This procedure yielded an estimate of Fisher Information for each numerosity n , separately for each participant and condition. These values quantify the acuity of the neural representation at different numerosities. We then used these measures to assess how manipulating the objective prior in the experiment altered the fidelity with which right NPC encoded numerosity across participants and conditions.

Expected Variability from an Ideal Bayesian Decoder

Fisher Information is a purely local measure: it reflects sensitivity to infinitesimal changes around a given n , but does not account for the discrete nature of number, boundary effects, or the impact of substantial noise⁹⁰. Indeed, in our data, Fisher Information failed to capture the increased precision at the edges of the tested numerosity range. To obtain a more realistic estimate of the expected variability of an actual neural decoder, we therefore complemented the Fisher Information analysis with simulations of an ideal Bayesian decoder. This approach allowed us to approximate the performance of a perfect decoder given the observed neural code, providing a more global measure of representational acuity.

We modeled voxel responses as a multivariate Gaussian distribution,

$$y \sim \mathcal{N}(f(n; \theta), \Sigma),$$

with mean given by the predicted nPRF responses $f(n; \theta)$ and covariance Σ estimated from the residuals of the best-fitting model. Using this generative model, we simulated large numbers of single-trial response patterns for each numerosity under both the Narrow and Wide stimulus ranges. For each simulated response y , we computed the Bayesian posterior over numerosities, $p(n | y)$, and decoded the stimulus as the posterior mean,

$$\hat{n} = \mathbb{E}[n | y].$$

Repeating this procedure many times yielded distributions of decoded numerosities for each true numerosity, from which we quantified variability, systematic bias, and absolute error. By correlating the variability of numerosities decoded from simulated data with the variability observed in participants' responses, we were able to test whether the precision of neural representations in right NPC predicts the precision of behavior.

Statistical analysis of the behavioral data

Figure 1b shows posterior mean estimates of the group-level parameters from a hierarchical model that includes participant-level random effects. For each condition, the model is defined by the following equations, where \hat{x}_{si} denotes the estimate of participant s in trial i , while x_i denotes the correct number:

$$\begin{aligned}\hat{x}_{si} \mid x_i &\sim N(m_s(x_i), \sigma_s(x_i)^2) \\ m_s(x) &\sim N(m_0(x), \tau^2), \\ \ln \sigma_s(x) &\sim N(\ln \sigma_0(x), \nu^2),\end{aligned}\tag{5}$$

with the priors

$$\begin{aligned}m_0(x) &\sim N(x, 10^2), \\ \sigma_0(x) &\sim N_+(3.5, 3.5^2) \\ \tau &\sim N_+(2, 5^2), \\ \text{and } \nu &\sim N_+(1, 2^2),\end{aligned}\tag{6}$$

where N_+ is the Gaussian distribution truncated to the positive numbers. This model was estimated using Stan⁹¹ (10 chains of 1000 samples each, following 1000 warmup iterations, with the HMC-NUTS sampler). The shaded areas in Figure 1b show the 5th and 95th percentile of the posterior.

Analysis code and data

All analysis code is available on GitHub at https://github.com/Gilles86/neural_priors. The fMRI data will be made publicly accessible on OpenNeuro. Meanwhile, requests can be addressed to the authors.

61. Barretto-García, M. *et al.* Individual risk attitudes arise from noise in neurocognitive magnitude representations. *Nature Human Behaviour* **7**, 1551–1567 (2023).
62. de Hollander, Gilles, Grueschow, M., Hennel, F. & Ruff, C. C. *Rapid Changes in Risk Preferences Originate from Bayesian Inference on Parietal Magnitude Representations* Aug. 2024.
63. de Hollander, Gilles, Moisa, M. & Ruff, C. C. *Risk Preferences Causally Rely on Parietal Magnitude Representations: Evidence from Combined TMS-fMRI* Jan. 2025.
64. Esteban, O. *et al.* fMRIPrep: a robust preprocessing pipeline for functional MRI. *Nature Methods* **16**, 111–116 (2019).
65. Esteban, O. *et al.* fMRIPrep. *Software* (2018).
66. Gorgolewski, K. *et al.* Nipype: a flexible, lightweight and extensible neuroimaging data processing framework in Python. *Frontiers in Neuroinformatics* **5**, 13 (2011).
67. Gorgolewski, K. J. *et al.* Nipype. *Software* (2018).
68. Andersson, J. L., Skare, S. & Ashburner, J. How to correct susceptibility distortions in spin-echo echo-planar images: application to diffusion tensor imaging. *NeuroImage* **20**, 870–888. ISSN: 1053-8119 (2003).
69. Tustison, N. J. *et al.* N4ITK: Improved N3 Bias Correction. *IEEE Transactions on Medical Imaging* **29**, 1310–1320. ISSN: 0278-0062 (2010).

70. Zhang, Y., Brady, M. & Smith, S. Segmentation of brain MR images through a hidden Markov random field model and the expectation-maximization algorithm. *IEEE Transactions on Medical Imaging* **20**, 45–57. issn: 0278-0062 (2001).
71. Reuter, M., Rosas, H. D. & Fischl, B. Highly accurate inverse consistent registration: A robust approach. *NeuroImage* **53**, 1181–1196 (2010).
72. Dale, A. M., Fischl, B. & Sereno, M. I. Cortical Surface-Based Analysis: I. Segmentation and Surface Reconstruction. *NeuroImage* **9**, 179–194. issn: 1053-8119 (1999).
73. Klein, A. *et al.* Mindboggling morphometry of human brains. *PLOS Computational Biology* **13**, e1005350. issn: 1553-7358 (2017).
74. Cirić, R. *et al.* TemplateFlow: FAIR-sharing of multi-scale, multi-species brain models. *Nature Methods* **19**, 1568–1571 (2022).
75. Fonov, V., Evans, A., McKinstry, R., Almlí, C. & Collins, D. Unbiased nonlinear average age-appropriate brain templates from birth to adulthood. *NeuroImage* **47**, Supplement 1, S102 (2009).
76. Jenkinson, M., Bannister, P., Brady, M. & Smith, S. Improved Optimization for the Robust and Accurate Linear Registration and Motion Correction of Brain Images. *NeuroImage* **17**, 825–841. issn: 1053-8119 (2002).
77. Greve, D. N. & Fischl, B. Accurate and robust brain image alignment using boundary-based registration. *NeuroImage* **48**, 63–72. issn: 1095-9572 (2009).
78. Power, J. D. *et al.* Methods to detect, characterize, and remove motion artifact in resting state fMRI. *NeuroImage* **84**, 320–341. issn: 1053-8119 (2014).
79. Abraham, A. *et al.* Machine learning for neuroimaging with scikit-learn. English. *Frontiers in Neuroinformatics* **8**. issn: 1662-5196 (2014).
80. Harvey, B. M., Klein, B. P., Petridou, N. & Dumoulin, S. O. Topographic Representation of Numerosity in the Human Parietal Cortex. *Science* **341**, 1123–1126. issn: 0036-8075 (2013).
81. Prince, J. S. *et al.* Improving the accuracy of single-trial fMRI response estimates using GLMsingle. *eLife* **11**. Structure Intro * New age in visual neuroscience, e77599 (2022).
82. Kay, K. N., Rokem, A., Winawer, J., Dougherty, R. F. & Wandell, B. A. GLMdnoise: a fast, automated technique for denoising task-based fMRI data. *Frontiers in Neuroscience* **7**, 247. issn: 1662-4548 (2013).
83. Kingma, D. P. & Ba, J. Adam: A Method for Stochastic Optimization. *ICLR 2015*. eprint: 1412.6980 (2014).
84. Abadi, M. *et al.* *TensorFlow: A system for large-scale machine learning* in *Proceedings of the 12th USENIX Symposium on Operating Systems Design and Implementation (OSDI)*. (Savannah, Georgia, 2016), 265–283.
85. Aqil, M., Knapen, T. & Dumoulin, S. O. Divisive normalization unifies disparate response signatures throughout the human visual hierarchy. *Proceedings of the National Academy of Sciences* **118**, e2108713118. issn: 0027-8424 (2021).
86. de Hollander, G., Renkert, M., Ruff, C. C. & Knapen, T. H. *Braincoder: A Package for Fitting Encoding Models to Neural Data and Decoding Stimulus Features* Zenodo. 2024.
87. Zhang, L.-Q., Mao, J., Aguirre, G. K. & Stocker, A. A. The tilt illusion arises from an efficient reallocation of neural coding resources at the contextual boundary. *Proceedings of the National Academy of Sciences* **122**, e2421565122. issn: 0027-8424 (2025).
88. Van Bergen, R. S., Ma, W. J., Pratte, M. S. & Jehee, J. F. M. Sensory uncertainty decoded from visual cortex predicts behavior. *Nature Neuroscience* **18**, 1728. issn: 1097-6256 (2015).
89. Ledoit, O. & Wolf, M. The Power of (Non-)Linear Shrinking: A Review and Guide to Covariance Matrix Estimation. *Journal of Financial Econometrics* **20**, 187–218. issn: 1479-8409 (2020).
90. Hahn, M. & Wei, X.-X. A unifying theory explains seemingly contradictory biases in perceptual estimation. *Nature Neuroscience*, 1–12. issn: 1097-6256 (2024).

91. Team, S. D. *Stan Modeling Language Users Guide and Reference Manual*, 2.35 2024.